JOURNAL OF PROPULSION AND POWER
Vol. 23, No. 2, March–April 2007

Visualization of Wave Rotor Inner Flow Dynamics

Koji Okamoto* and Toshio Nagashima†
University of Tokyo, Tokyo 113-8656, Japan

DOI: 10.2514/1.18439

The design of a wave rotor requires an understanding of the pressure wave dynamics in the cells (rotor passages). The present paper describes a two-dimensional numerical simulation and an experimental visualization of the wave rotor compression process. First, a unique experimental apparatus with fixed cells and rotating ports was constructed for the visualization and direct measurements; this arrangement is opposite to the conventional setup. Next, experimental and numerical results were compared to verify the simulation modeling, particularly with regard to the propagation velocity of pressure waves in the cells. Last, the effects of gradually opening the cell to the ports and leakage through the clearance, which are considered to be dominant factors in the wave rotor operation, on the pressure wave dynamics were carefully investigated. The results showed that the gradual passage opening greatly influences the primary shock wave, whereas leakage mostly influences the reflected shock wave. Moreover, it was revealed that the leakage generates an extra pressure wave during the compression process due to the interaction between adjacent cells.

Introduction

THE wave rotor is a promising device that can drastically improve gas turbine performance [1–4]. It consists of a rotor and ducts, as shown in Fig. 1, and has multiple straight passages (cells) in which the energy of a combustion gas is directly transferred to air at a lower energy by means of unsteady pressure wave propagation. The ducts, hereafter referred to as "ports," are connected to the gas turbine components for charging and discharging the cells with fresh air and combustion gas, respectively.

Figure 2 shows the basic compression process of the "four-port reverse flow type" wave rotor cycle; the characteristic lines of the pressure waves are indicated by solid lines. An explanation of the entire working process can be found in the literature [5]. At the beginning of the cycle (top of the figure), the cell is filled with low pressure air from the compressor. Gas high pressure port (Gas-HP) is used to charge the combustion gas from the burner, and the pressure ratio of gas to air is greater than a suitable value (about 2.0 in [5]) for generating a shock wave (primary shock wave) when the cell is opened to Gas-HP. This shock wave is reflected at the opposite end of the cell, thereby generating another shock wave (reflected shock wave). Air high pressure port (Air-HP) is opened to the cell immediately after the reflection of this shock wave so that the high pressure air in the cell, which was compressed by these two shock waves, flows out to Air-HP. When the reflected shock wave reaches the end of the cell, Gas-HP is closed and an expansion wave is generated by the inertia of the inflow gas. Air-HP is closed when the tail of this expansion wave reaches the end of the cell and the flow discharge is halted. Because the contact surface between the gas and air does not reach the end of the air side, the fluid in Air-HP is pure compressed air. The basic compression process of other wave rotor cycles [6,7] is very similar to this; however, some other applications use different compression process [8]. As seen in the aforementioned compression process, the ports should be opened and closed to coincide precisely with the pressure wave arrivals at the end of the cells. Therefore, the propagation velocity of the pressure waves in the cells must be predicted carefully, because the inner flow dynamics of the wave rotors differs greatly from those of an ideal shock tube because of some characteristic loss factors mentioned later.

A number of studies have aimed to develop an effective wave rotor design. These studies have employed analytical cycle calculations [4,9–12], one-dimensional (1-D) full-cycle simulations [13–15], two-dimensional (2-D) and three-dimensional (3-D) numerical analyses [16,17], and various experiments [18,19]. Experimental examinations [18,19] have revealed that the loss factors of the wave rotor performance can be classified as follows: gradual passage opening, (wall) friction, leakage (clearance), heat transfer, and so on. Here, gradual passage opening implies that the cells are gradually opened and closed to the ports; this is in contrast to an ideal shock tube in which the diaphragm is ruptured instantaneously.

These dominant factors are believed to influence significantly the process of pressure wave dynamics. For example, the primary shock wave may be a compression wave at the beginning of propagation because of the gradual passage opening effect. The compression wave is gradually strengthened during propagation, thereby leading to a nonlinear change in the propagation velocity; this contrasts with the observations obtained with an ideal shock tube. In addition, the reflection of the primary shock wave is not perfect because air flows out through the clearance gaps between the rotor and the end wall at the ends of cell; hence, it is difficult to analytically predict the condition of the reflected shock wave. Therefore, for developing an effective design technique, it is important to understand how these dominant factors affect the pressure wave dynamics.

As mentioned, one of the important points is the propagation velocity of the shock waves; however, experimental work employing optical visualization to investigate the generation and propagation process of shock waves has hardly been carried out. Therefore, both numerical simulations and experiments were performed to examine the effects of the gradual passage opening and leakage on the wave rotor compression process in the present study. In the experiments, shock wave visualization and direct pressure measurements were simultaneously carried out to clarify the generation and propagation of pressure waves. For comparison with the experimental results, a 2-D numerical simulation was performed on a peripheral plane located at the mean rotor radius.

Experimental Approach

Equipment

The shock waves in a wave rotor were visualized by using a new type of test equipment (Fig. 3) [20,21]. In this equipment, the cell is held stationary while the ports rotate. Hence, the reflecting schlieren method can be applied, and wall static pressure measurements can be directly performed without much difficulty. Thus, the effects of

---

Received 28 June 2005; revision received 5 April 2006; accepted for publication 20 April 2006.

*Research Associate, Department of Aeronautics and Astronautics, 7-3-1 Hongo, Bunkyo-ku.

†Professor, Department of Aeronautics and Astronautics, 7-3-1 Hongo, Bunkyo-ku.

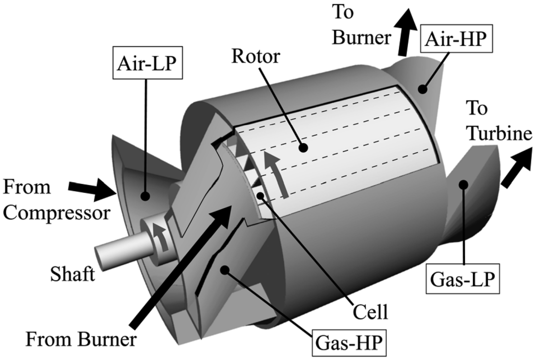

Fig. 1 Schematic diagram of wave rotor.

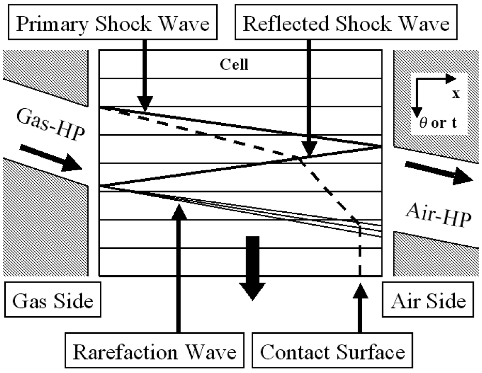

Fig. 2 Compression process of wave rotor.

rotation such as centrifugal and Coriolis forces were not taken into account; however, according to the 3-D numerical analysis, this effect will appear on the contact surface rather than the pressure waves [17]. With regard to the incidence loss between the rotating ports and fixed cells, the inflow angle from Gas-HP will be less than 10 deg thus making the loss insignificant [22]. It should be noted that the rotors shown in Fig. 3 indicate the rotating ports used for charging and discharging the working gas. These rotors were connected to a bevel gear and driven by an electric motor, and the test section can be replaced depending on the purpose of the experiments. The design specifications of this equipment are listed in Table 1. The initial design was made considering the theoretical propagation velocity of pressure waves, and then it was carefully adjusted according to the results of several test runs. The concept of this equipment was adopted for easy measurements and setting to make it suitable for the purpose of the present experiments and not for examining its performance as a fluid device. This is because of a limited number of cells that cannot deal with the full operation of the wave rotor.

The present design specifications were chosen mainly because of the tolerance available for the setup of the rotating parts. A comparison with the other wave rotors of previous studies [5,7,14,19,23] with regard to three nondimensional parameters that express the dominant loss factors of gradual passage opening, wall friction, and leakage is presented in Table 2. The three parameters are expressed as follows:

Gradual passage opening:
$\tau =$ (Passage Opening Time)/(Wave Travel Time) $= (W_{\mathrm{cell}}/r\omega)/(L/a)$

Wall friction: L/D_h

Leakage: $2\delta/H_{\mathrm{cell}}$

W_{cell} is the cell width; r, the mean rotor radius; ω, the angular speed of the rotor; a, the speed of sound; L, the cell length; D_h, the hydraulic diameter of the cell; δ, the axial clearance gap between the fixed end wall and the rotor, and H_{cell}, the cell height. The larger the value of these parameters, the larger is the performance loss. In the case of the cells with a width of 8 mm, τ does not differ much from the others; however, τ has the maximum value in the case of those with a width of 16 mm. The value of L/D_h yields identical values in the present design. As for $2\delta/H_{\mathrm{cell}}$, for a 0.5 mm clearance, the value appears fairly equal, whereas it is extremely large for a clearance of 1.0 mm.

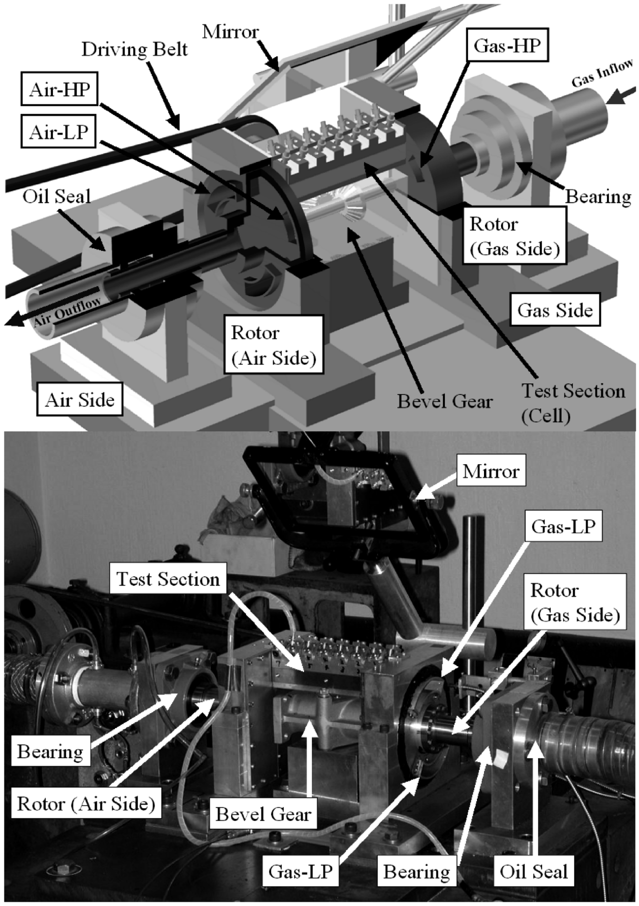

Fig. 3 Equipment for shock wave visualization.

Working Gas Charge and Discharge

The opening and closing timings of the ports are listed in Table 3. The origin (0.0 deg) indicates the beginning of a rotating cycle (i.e., Gas-HP opening). The four-port reverse flow cycle was adopted for the port configuration; this cycle is identical to that of the practical wave rotor for supercharging diesel engines [5]. Therefore, the gas side rotor, as shown in Fig. 3, has Gas-HP and gas low pressure port (Gas-LP), whereas the air side rotor has Air-HP and air low pressure port (Air-LP).

In this experiment, compressed air, hereafter referred to as gas, was supplied to Gas-HP. The pressure ratio of the gas to low pressure fresh air was 2.6, and their temperatures were equal to the room temperature. Gas pressurization was achieved using a screw compressor. The gas passed through a hollow rotating shaft and into the cell through Gas-HP. Shock waves were generated by the high pressure gas, which then flowed out into the atmosphere through Gas-LP of the gas side rotor. On the other hand, fresh air flowed into the cell through Air-LP, and it was compressed by the shock waves.

Table 1 Design specifications

Cell length	186 mm
Cell height	16 mm
Cell width	8 mm or 16 mm
Rotor mean radius	60 mm
Rotating speed	4200 rpm
Pressure ratio of Gas-HP and Air-LP	2.6
Wall thickness between cells	1.0 mm
Clearance	0.5–1.0 mm (variable)

Table 2 Comparison of wave rotor configurations

	NASA (3-port)	NASA & Allison	Kentfield	G.E.	Comprex® (ABB)	Visualization Test Rig (This work)
Length, L, m	0.23, 0.46	0.152	0.28	0.3	0.0932	0.186
Mean Radius, r, m	0.15	0.0815	0.102	0.058	0.048	0.06
Cell width, W_{cell}, m	0.00635, 0.0127	0.00875	0.0168	0.01[a]	0.009	0.008, 0.016
Cell height, H_{cell}, m	0.0102	0.022	0.0559	0.0231	0.01	0.016
Clearance, δ, mm	0.127–0.381	0.13	0.18	0.64	0.15	0.5–1.0
Rotating speed, rpm	1850–7400	16,800	5500	19,000	14,000	4200
τ	0.08–0.35	0.194	0.35	0.0982[b]	0.467	0.554, 1.108
L/D_h[c]	20–58	12.1	10.5	21.5	9.8	17.4, 11.6
$2\delta/H_{\mathrm{cell}}$	0.025–0.075	0.0118	0.006	0.0554	0.03	0.0625–0.125

[a] Wall thickness between the cells included.
[b] Calculated with atmospheric value.
[c] D_h: hydraulic diameter.

Table 3 Port design

Port	Opening timing, deg	Closing timing, deg
Gas-HP	0.0	29.0
Gas-LP	60.0	158.0
Air-HP	13.0	39.5
Air-LP	77.2	132.2

Subsequently, air flowed into Air-HP and then to the atmosphere through the rotating shaft of the air side rotor.

Optical and Pressure Measurements

Optical observation was performed using the reflecting schlieren method. The path of the light beam was set horizontally and directed downward by a mirror placed above the test section. Light passed from the top of the test section to its bottom, and it was reflected by another mirror placed below the test section. To avoid mechanical vibrations, the test section and mirrors were isolated from the rotating parts such as the bevel gear, bearings, and oil seals, as shown in Fig. 3. In this experiment, a high speed CCD camera with a shutter speed of 500 ns was used to capture schlieren photographs. The trigger pulse, which marked the beginning of the cycle, controlled the camera so that a series of pictures was recorded as tiff files using a computer. For measuring the wall static pressure, seven holes with flush-mounted dynamic pressure transducers were arranged in the axial direction along each side of the top transparent plate. The resonance frequency of the pressure transducer was 400 kHz, and the frequency response of the dc amplifier was 0–100 kHz with an attenuation less than 3 dB. In this experiment, signal filtering was not employed and the data were obtained with a digital oscilloscope that produced 5 mega samples per second for each channel.

Figure 4 shows the details of the test section and the measuring points. Leakage flows at the interface of the cells and ports can be considered to occur in both radial and circumferential directions. The leakage flow in the radial direction merely leaks out to the ambient air, whereas that in the circumferential direction causes an interaction between the adjacent cells. Therefore, the test section was arranged to have three cells, and optical and pressure measurements were carried out at the central cell for observing the interaction between the cells. The top and bottom walls of the central cell were made of transparent acrylic resin. For examining a single passage, the gas and air were supplied only to the central cell by changing the end walls that support both the ends of the test section. In addition, a 16 mm wide test section (single passage only) was also used to examine the effect of gradual passage opening.

Numerical Approach

Solution Method

In the present study, a 2-D analysis was performed at the mean radius plane (developed in the cell axis and rotating directions) by focusing on the dynamics of the primary and reflected shock waves in the compression process [20,21]. As easily seen from the relation between the calculation plane and the rotating axis, the effects of the centrifugal and Coriolis forces were not taken into consideration. Two-dimensional Navier–Stokes equations considering laminar viscosity were used as the governing equations. The solution scheme was based on the finite difference method of discretization by incorporating Chakravarthy–Osher's third-order upwind total variation diminishing (TVD) scheme with van Leer's differentiable limiter [24,25]. Jameson–Baker's four-stage Runge–Kutta scheme (fourth-order accuracy) was employed for time integration [26]. The time step was estimated from the maximum CFL number, which was set to 1.0. This numerical scheme has been improved and applied for a long time in various types of flowfields [27–33]. It was also validated by the results of the ideal shock tube problem by using the Exact Riemann Solver [34].

Calculation Region

Figure 5 illustrates the mesh used for simulating the cell-to-cell interaction effect. This mesh covers the region of the three passages, similar to the test section in the experiment, and each cell region consists of 601 × 31 orthogonal grids. The specifications of each cell were identical to those in the experiment, i.e., the cell widths for examining the effect of gradual passage opening were 8 and 16 mm, as listed in Table 1. The cells were connected to each other through

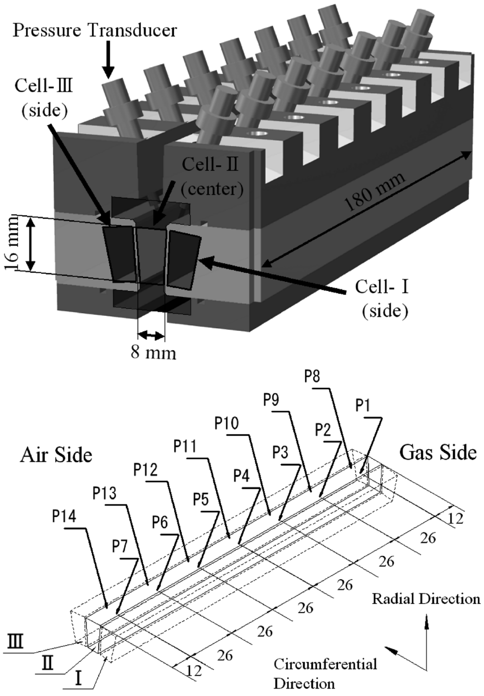

Fig. 4 Test section and measuring points (unit: mm).

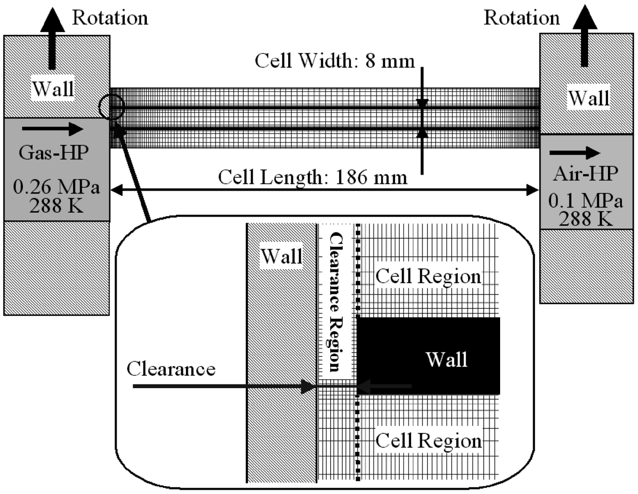

Fig. 5 Calculation region (multipassage case).

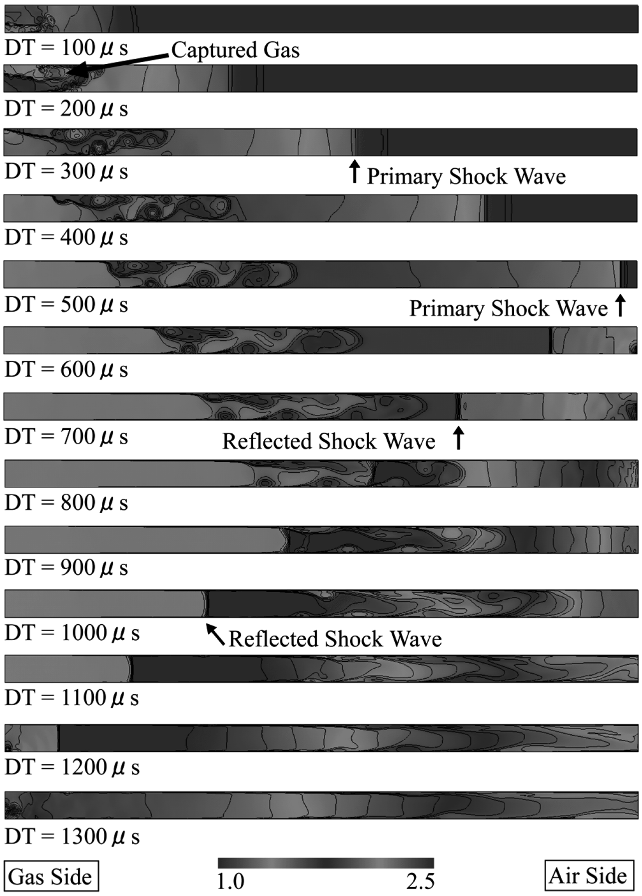

Fig. 6 Density contours (Case 1).

the clearance region, which was delineated by the grids in the cell region. The results obtained using clearances of 0.5 and 1.0 mm were compared to investigate the leakage effect. Here, because the condition in the port was assumed to be uniform and constant, disturbances within the port arising from the multipassage effect were not taken into account. In the single-passage simulation without the leakage effect, only the cell region was considered; therefore, the inflow and outflow boundary conditions were directly applied to the cell ends. In contrast, in the presence of leakage without any interaction effects, the clearance region was attached to each cell end, and its length was equal to the cell width in the circumferential direction. To investigate the effect of gradual passage opening, a 601×61 mesh (doubled grids in the circumferential direction) was also employed in the case of the 16 mm cell width for maintaining the same grid accuracy. All the calculation cases presented in this paper are shown in Table 4.

Boundary Conditions

The inflow and outflow boundary conditions must be carefully treated because the flow direction and flow velocity, supersonic or subsonic, are not known a priori. Therefore, a phantom point was set outside each boundary grid, and the local 1-D (axial direction) Riemann problem was solved for this phantom point and its corresponding boundary point by applying the Exact Riemann Solver for obtaining appropriate boundary values [34]. First, the kind of pressure wave (shock wave or expansion wave) that travels either in the left or right direction from the interface was determined according to the conditions of the internal and phantom points. Then, the condition between these two (left and right running) pressure waves was calculated using the relation for a shock or expansion wave. Finally, the flux at the interface was obtained and applied as the boundary condition. In this way, the boundary condition was determined according to the direction of two characteristic lines of the pressure waves from the interface.

The port states are imposed at the appropriate phantom points. In the present simulation, the condition in each port was assumed to be constant; otherwise, for the simulation, it would be necessary to solve for all the cells simultaneously including the port region. Therefore, the total and static pressures in Gas-HP were measured with a pitot tube in the preliminary experiment to set an appropriate Gas-HP boundary condition. Table 5 lists the port conditions for the numerical simulation that were identical to those in the experiments. Here, the circumferential velocity in Gas-HP was assumed to be the same as the rotor peripheral speed at the mean radius, and it was imposed directly at the boundary points. In addition, the opening and closing timings of the ports were the same as those in the experiment. The effect of gradual passage opening was simulated by gradually replacing the wall boundary condition by the corresponding port boundary condition; this is in accordance with the cell rotation. Nonslip and adiabatic conditions were applied to the wall boundary and the cell walls; therefore, the effect of heat transfer was not considered in the present simulation. The initial condition of pressure, temperature, and velocity in the cell was set as 0.1 MPa, 288 K, and 0 m/s, respectively.

In the simulation considering the leakage effect, the leakage flow through the clearance region in the radial direction, i.e., normal to the calculation plane, should also be considered. In the present simulation, each calculation volume was treated as a cube of 16 mm height that was identical to the value in the experiment. Then, the fluxes at the top and bottom interfaces with the outside ambient air were similarly calculated by the Exact Riemann Solver [34]. By assuming the flow to be symmetric in both the inner and outer radial directions, the amount of leakage flow was then taken into account at each time step for calculating the new condition for the next time step. At the boundary of the clearance region in the circumferential

Table 4 Calculation case

	Case 1	Case 2	Case 3	Case 4	Case 5
Passage number	1	1	1	3	3
Width	8 mm	8 mm	16 mm	8 mm	8 mm
Clearance	0 mm	0.7 mm	0 mm	0.5 mm	1.0 mm

Table 5 Port conditions

	Gas-HP	Air-HP
Total pressure, MPa	0.26	0.1
Total temperature, K	288	288
Velocity, m/s (axial)	160	0.0
Velocity, m/s (circumferential)	26.4	0.0

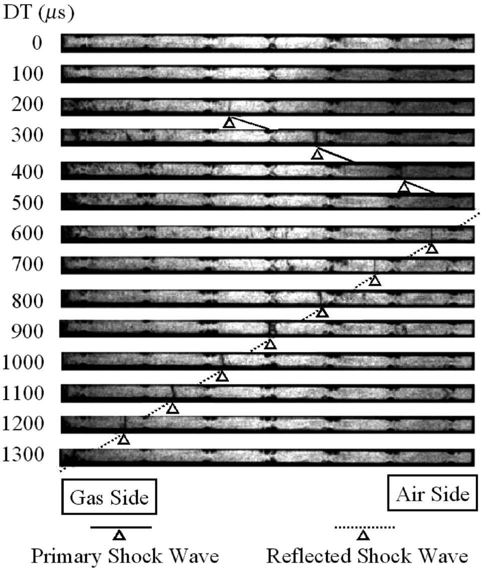

Fig. 7 Schlieren photographs (single-passage case).

direction (top and bottom boundary of the clearance regions in Fig. 5), the wall condition was adopted in the multipassage simulations; this is because the periodic boundary condition in the circumferential direction cannot be applied without solving for all the cells that cover the entire cycle. This treatment was previously confirmed to be appropriate by comparing the results of three- and five-passage simulations in which no significant difference was found. In the case of the single-passage simulation with the leakage flow effect (Case 2 in Table 4), the boundary condition of the clearance region in the circumferential direction was treated to be open to the surroundings.

Results

Wave Visualization and Computed Density Contour

Figure 6 shows the time series of the computed nondimensional density contours in the case of the single-passage simulation without the leakage effect (Case 1). In this figure, delay time (DT) indicates the time elapsed from the instant Gas-HP begins to open upward from the bottom at the left cell end.

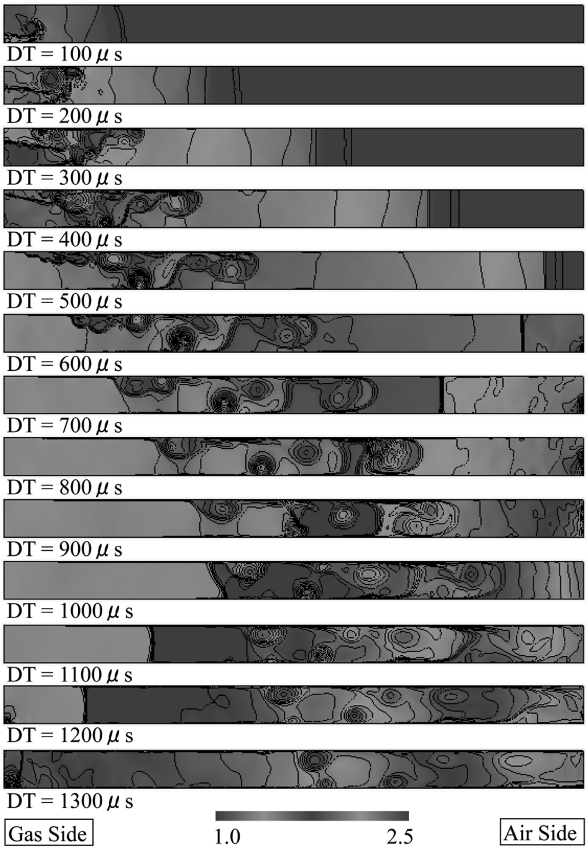

Fig. 9 Density contours (Case 3).

When Gas-HP begins to open, a compression wave and contact surface are generated and they propagate to the air side. The shape of this compression wave appears to be one-dimensional even at DT = 100 μs, although Gas-HP is completely opened at DT= 303 μs. At the instant Gas-HP begins to open, its shape is cylindrical and becomes flat immediately. Then, the wave is gradually strengthened during propagation and finally becomes a primary shock wave. Regarding the contact surface, the inflow is attached to the upper wall of the cell; thus, a region denoted as "captured gas" is

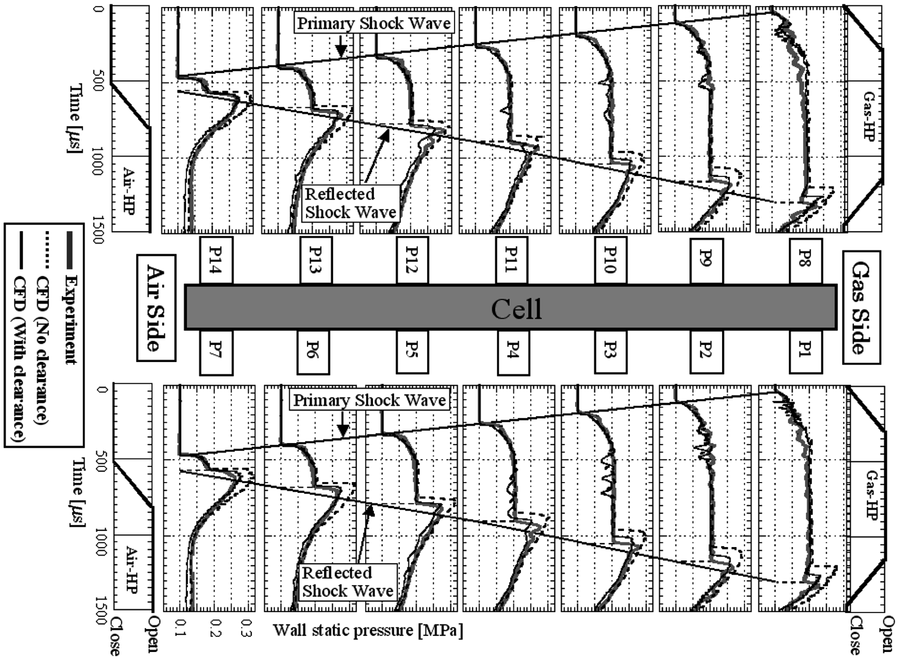

Fig. 8 Experimental and simulated wall static pressure traces (single-passage cases).

Table 6 Propagation velocity of shock waves

	Primary shock wave	Reflected shock wave
Experiment	358 m/s	218 m/s
CFD (Case 1)	368 m/s	253 m/s
CFD (Case 2)	368 m/s	236 m/s

formed near the upper corner of the cell entrance (DT = 200 μs). The primary shock wave then propagates and reflects at the end of the air side (DT = 600 μs). At this instant, Air-HP is partially opened to the cell (Air-HP begins to open at DT = 516 μs), and a small amount of compressed air flows out to Air-HP. The reflected shock wave propagates against the inflow to the gas side to interact with the contact surface. When it reaches the end of the gas side, Gas-HP begins to close at DT = 1151 μs, resulting in a low pressure area (DT = 1300 μs).

Figure 7 shows the schlieren photographs obtained from the single-passage experiments with a 0.5 mm clearance. As shown in this figure, the primary shock wave is not observed at DT = 100 μs because the density gradient of the shock wave at this instant is not sufficiently strong due to the effect of gradual passage opening. The primary shock wave becomes apparent after DT = 200 μs, and it is reflected at approximately DT = 500 μs. In addition, it can be clearly seen that the reflected shock wave propagates to the gas side at a constant speed.

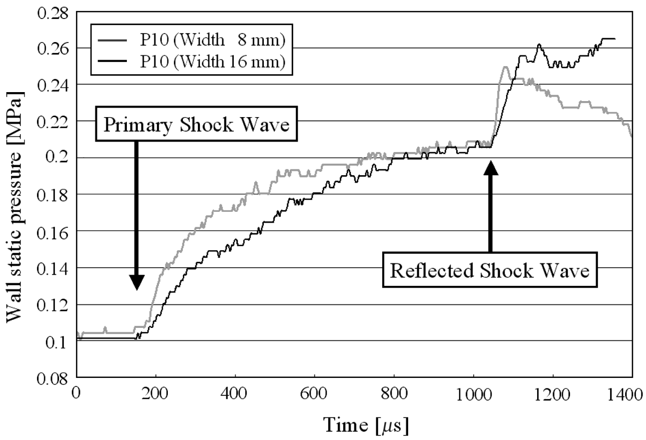

Fig. 10 Static pressure time trace at P10 (experimental).

Comparison of Numerical and Experimental Results

Figure 8 shows a comparison of the numerical (Cases 1 and 2) and experimental results for the wall static pressure traces in the single-passage case. The numerical result considering the clearance (Case 2) takes into account only the effect of the leakage flow to the outside.

This comparison shows that the leakage flow to the outside significantly influences the strength and propagation velocity of the reflected shock wave. In contrast, the primary shock wave was not noticeably affected. In terms of both the propagation velocity and pressure ratio of the shock waves, the numerical results for the case in which the leakage effect is considered show a better agreement with the measurements than the case in which the leakage effect is not considered. This indicates the practical importance of taking the presence of the clearance into account. Table 6 presents a summary of the propagation velocities of the primary and reflected shock waves, which quantitatively supports the aforementioned finding.

Gradual Passage Opening Effect

In the present discussion, cells with widths of 8 and 16 mm were tested to compare the results obtained by the numerical simulation with those obtained experimentally. All the design and operating conditions, excluding the cell width, were identical. Therefore, as shown in Table 2, the value of τ was doubled, revealing the differences due to an increase in the effect of gradual passage opening. Meanwhile, in the numerical simulation, the clearance was set to zero to eliminate the leakage effect. It is generally supposed that τ should be less than 1.0, and it was less than 0.5 in the other previously designed wave rotors. Therefore, a width of 16 mm for a cell is too large and this extreme case was designed only to observe the effect of gradual passage opening.

Figure 9 shows the computed density contours of the 16 mm wide cell (Case 3). As seen in this figure, the primary shock wave cannot be observed as clearly as in the case of the 8 mm wide cell shown in Fig. 6; however, the reflected shock wave appears to be sufficiently clear. This trend is also observed in the comparison of the wall pressure measurements in the experiments of different cell widths (Fig. 10). In the case of the 16 mm wide cell, the rate of increase in pressure of the primary shock wave reduces, whereas that of the reflected shock wave remains almost constant. Consequently, the

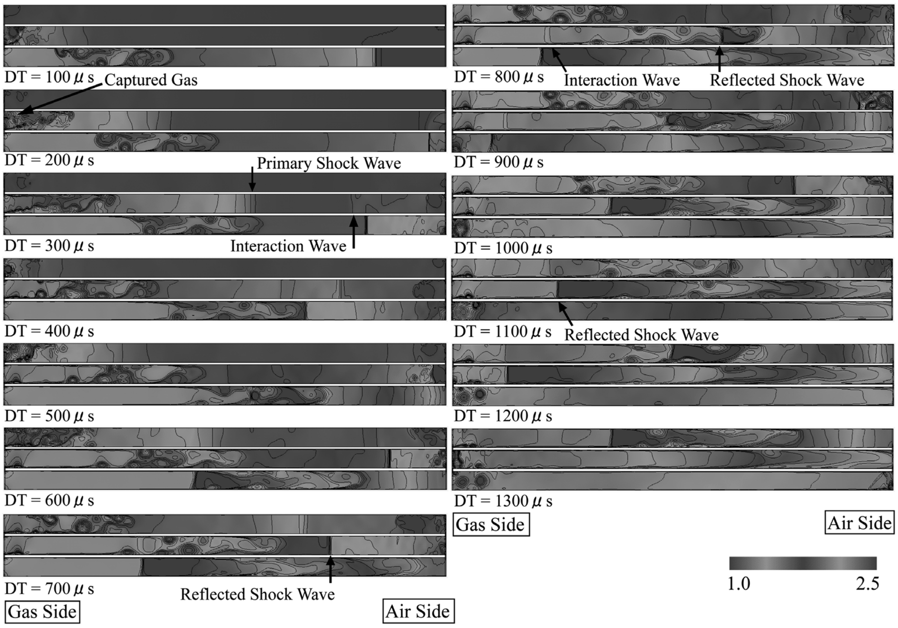

Fig. 11 Density contours (Case 4).

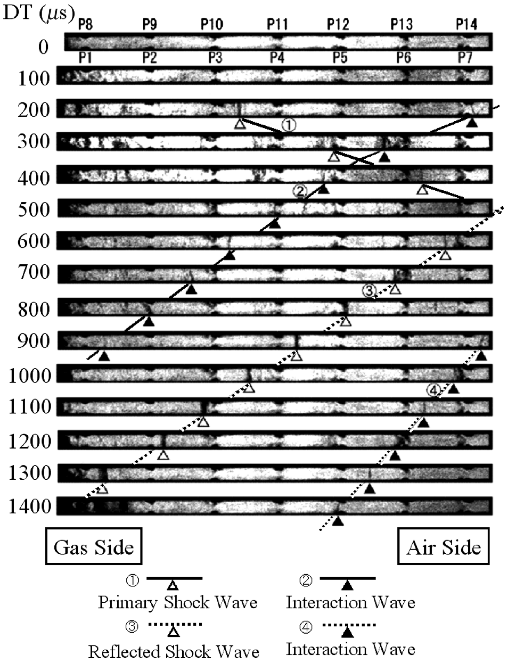

Fig. 12 Schlieren photographs (three-passage case, clearance 0.5 mm).

gradual passage opening has a greater influence on the primary shock wave than the reflected shock wave.

Leakage Effect

The time series of nondimensional density contours of the multipassage simulation (Case 4) is shown in Fig. 11. In this figure, the origin of DT indicates the instant at which Gas-HP begins to open with respect to the middle cell. In addition to the result for the single passage (Fig. 6), it is observed that an extra wave, hereafter referred to as the interaction wave, is generated in the middle cell. The interaction wave then propagates to the gas side. This phenomenon is also observed in the schlieren photographs in Fig. 12, which were taken during the three-passage experiment. On the basis of the generation timing and numerical results, this pressure wave appears to have been generated by the reflection of the primary shock wave at the cell end of the neighboring cell (bottom) that had earlier opened to Gas-HP (Fig. 13).

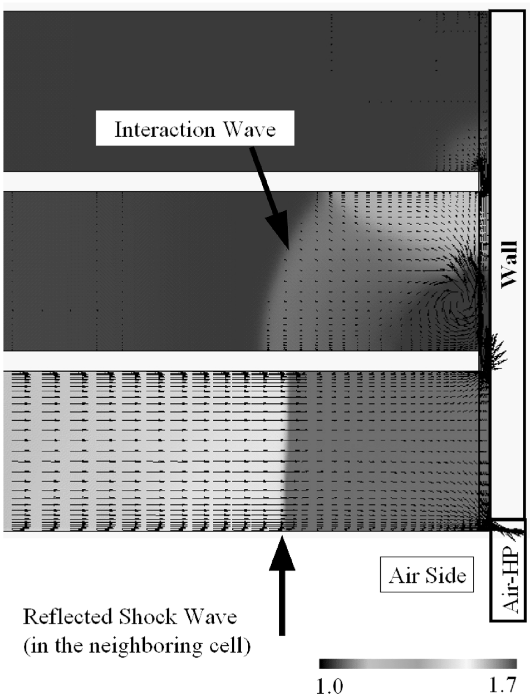

Fig. 13 Interaction wave generation (Case 4).

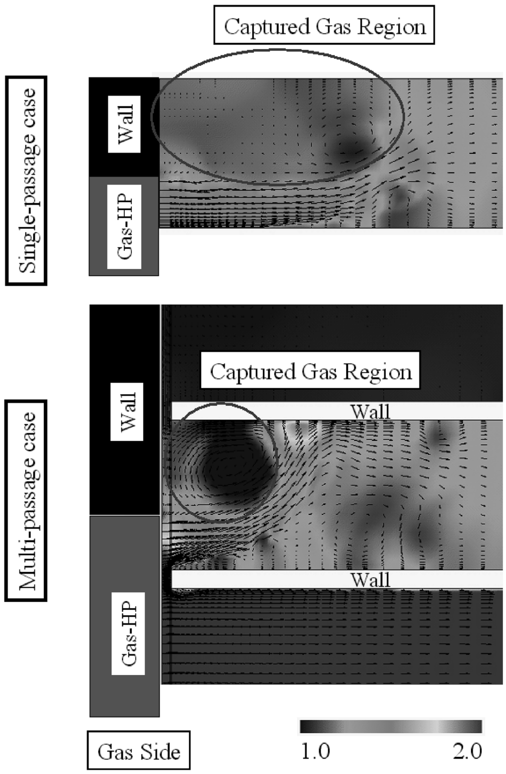

Fig. 14 Inflow difference between Cases 1 and 4.

In addition, the state of the contact surface in the three-passage simulation is very different from that in the single-passage simulation owing to the difference in the inflow angle at the beginning of Gas-HP opening (Fig. 14). In the single-passage case, the inflow direction was almost axial; the flow was diverted by a vortex and finally reattached to the upper wall, thus forming the captured gas region (Fig. 6). On the other hand, in the multipassage case, the inflow angle was greater because the flow direction around the leading edge was almost circumferential. Therefore, the captured gas region is not very evident in this case.

Figure 15 shows the numerical results for the wall static pressure traces corresponding to clearances of 0.0, 0.5, and 1.0 mm (Cases 1, 4, and 5). Here, the clearance of 0 mm corresponds to the single-passage simulation without the leakage effect. Further, note that a

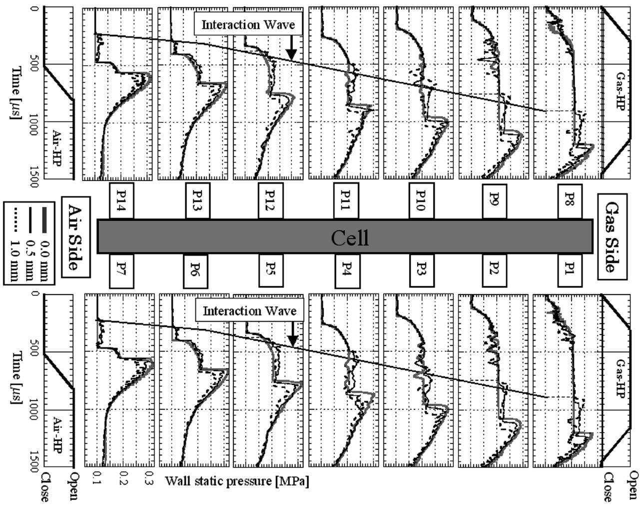

Fig. 15 Wall static pressure traces (Cases 1, 4, and 5).

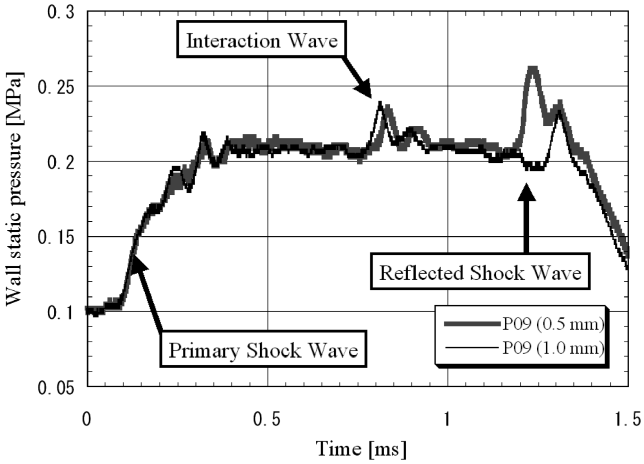

Fig. 16 Pressure traces for different clearances (experimental).

clearance of 1.0 mm yields an extremely large value of the leakage parameter, which is used only to observe the limiting influence of a large clearance. The strength of the reflected shock wave and interaction wave were again observed to be greatly influenced by the clearance width. In particular, when the clearance was 1.0 mm, the strength of the interaction wave was almost the same as that of the reflected shock wave; therefore, the interaction wave cannot be neglected in the extreme case in which the leakage parameter is large. This observation is also confirmed by the experimental results (Fig. 16). Moreover, the propagation velocity of the interaction wave changed at P5 and P12 due to interference with the primary shock wave.

Figure 15 also reveals that a difference in the inflow angle resulted in a difference in the initial increase in pressure at P1 and P8. Without a clearance, a sudden decrease during the initial increase in pressure at P8 is due to the captured gas region, which does not appear otherwise. The influence of this difference in the inflow angle was only local and was not observed at other measuring points. The propagation velocities of the reflected shock wave are compared in Table 7. The difference among the three clearance cases examined in this study was found to be 20%.

To determine the influence of the number of cells, a simulation with five cells was also performed. It was concluded that the simulation with three cells is adequate for the present discussion.

Conclusions

In the present study, wave rotor inner flow dynamics were investigated both experimentally and numerically. A unique apparatus was constructed for the experiment, in which the propagating shock and pressure waves within the cell passages were visualized for the first time. Furthermore, the propagation velocities were examined based on the time traces of the wall static pressure. In the numerical analysis, a 2-D flow simulation was performed; the results were compared with the experimental data in terms of the propagation velocities and steepness of the shock waves, which are critically important in wave rotor design. The principal results and conclusions regarding the specific aspects of the wave rotor operation are as follows.

1) The effect of gradual passage opening was clear in the steepness of the primary shock wave and the state of the contact discontinuity, whereas the reflected shock wave was not affected.

Table 7 Propagation velocity of reflected shock wave (numerical)

	Case 1	Case 4	Case 5
Clearance	0 mm	0.5 mm	1.0 mm
Propagation velocity	253 m/s	236 m/s	214 m/s

2) The leakage effect can be considered as a leakage flow to the surroundings and the interaction between neighboring cells. The leakage flow appeared to affect the pressure ratio of the reflected shock wave, whereas the primary shock wave did not seem to be affected.

3) The cell-to-cell interaction effect appeared as an interaction wave, which was generated by the reflection of the primary shock wave at the end of an adjacent cell. When the clearance was increased to an extreme, the strength of this interaction wave became almost equal to that of the reflected shock wave. Therefore, this effect can be significant in such a configuration.

4) The inflow angle of the high pressure gas is significantly affected by the leading edges of the cell walls; this significantly influences the contact surface states with regard to the formation and structure of the flow circulation at the cell entrance.

References

[1] Welch, G. E., Jones, S. M., and Paxson, D. E., "Wave-Rotor-Enhanced Gas Turbine Engines," *Journal of Engineering for Gas Turbines and Power*, Vol. 119, No. 2, April 1997, pp. 469–477.

[2] Wilson, J., and Paxson, D. E., "Wave Rotor Optimization for Gas Turbine Engine Topping Cycles," *Journal of Propulsion and Power*, Vol. 12, No. 4, July–Aug. 1996, pp. 778–785.

[3] Welch, G. E., Paxson, D. E., Wilson, J., and Snyder, P. H., "Wave-Rotor-Enhanced Gas Turbine Engine Demonstrator," NASA, TM-1999-209459, Oct. 1999.

[4] Fatsis, A., and Ribaud, Y., "Thermodynamic Analysis of Gas Turbines Topped with Wave Rotors," *Aerospace Science and Technology*, No. 5, 1999, pp. 293–299.

[5] Gyarmathy, G., "How Does the Comprex® Pressure-Wave Supercharger Work?" Society of Automotive Engineers Technical Paper 830234, 1983.

[6] Kentfield, J. A. C., "Wave-Rotors and Highlights of Their Development," AIAA Paper 98-3248, July 1998.

[7] Snyder, P. H., and Fish, R. E., "Assessment of a Wave Rotor Topped Demonstrator Gas Turbine Engine Concept," American Society of Mechanical Engineers Paper 96-GT-41, June 1996.

[8] Nalim, M. R., "Longitudinally Stratified Combustion in Wave Rotors," *Journal of Propulsion and Power*, Vol. 16, No. 6, Nov.–Dec. 2000, pp. 1060–1068.

[9] Wilson, J., and Paxson, D. E., "Jet Engine Performance Enhancement Through use of a Wave-Rotor Topping Cycle," NASA Technical Memorandum 4486, 1993.

[10] Resler, E. L., Jr., Mocsari, J. C., and Nalim, M. R., "Analytic Design Methods for Wave Rotor Cycles," *Journal of Propulsion and Power*, Vol. 10, No. 5, Sept.–Oct. 1994, pp. 683–689.

[11] Nalim, M. R., "Thermodynamic Limits of Work and Pressure Gain in Combustion and Evaporation Processes," *Journal of Propulsion and Power*, Vol. 18, No. 6, Nov.–Dec. 2002, pp. 1176–1182.

[12] Akbari, P., and Muller, N., "Preliminary Design Procedure for Gas Turbine Topping Reverse-Flow Wave Rotors," FR-301, *Proceedings of the International Gas Turbine Congress*, Tokyo, Nov. 2003.

[13] Paxson, D. E., and Wilson, J., "An Improved Numerical Model for Wave Rotor Design and Analysis," AIAA Paper 93-0482, Jan. 1993.

[14] Paxson, D. E., "Comparison Between Numerically Modeled and Experimentally Measured Wave-Rotor Loss Mechanisms," *Journal of Propulsion and Power*, Vol. 11, No. 5, Sept.–Oct. 1995, pp. 908–914.

[15] Fatsis, A., Lafond, A., and Ribaud, Y., "Preliminary Analysis of the Flow Inside a Three-Port Wave Rotor by Means of a Numerical Model," *Aerospace Science and Technology*, No. 5, 1998, pp. 289–300.

[16] Welch, G. E., "Two-Dimensional Computational Model for Wave Rotor Flow Dynamics," *Journal of Engineering for Gas Turbines and Power*, Vol. 119, Oct. 1997, pp. 978–985.

[17] Larosiliere, L. M., "Wave Rotor Charging Process: Effects of Gradual Opening and Rotation," *Journal of Propulsion and Power*, Vol. 11, No. 1, Jan.–Feb. 1995, pp. 178–184.

[18] Wilson, J., and Fronek, D., "Initial Results From the NASA-Lewis Wave Rotor Experiment," AIAA Paper 93-2521, June 1993.

[19] Wilson, J., "An Experimental Determination of Losses in a Three-Port Wave Rotor," *Journal of Engineering for Gas Turbines and Power*, Vol. 120, Oct. 1998, pp. 833–842.

[20] Okamoto, K., Nagashima, T., and Yamaguchi, K., "Rotor-Wall

Clearance Effects upon Wave Rotor Passage Flow," International Symposium on Air Breathing Engines (ISABE) Paper 2001-1222, Sept. 2001.

[21] Nagashima, T., Okamoto, K., and Ribaud, Y., "Cycles and Thermal System Integration Issues of Ultra-Micro Gas Turbines," RTO-EN-AVT-131, *AVT/VKI Lecture Series on Micro Gas Turbines*, von Karmán Institute, Belgium, March 2005.

[22] Paxson, D. E., "An Incidence Loss Model for Wave Rotors With Axially Aligned Passages," AIAA Paper 98-3251, July 1998.

[23] Snyder, P. H., "Wave Rotor Demonstrator Engine Assessment," NASA Contractor Report 198496, June 1996.

[24] Chakravarthy, S. R., and Osher, S., "A New Class of High Accuracy TVD Schemes for Hyperbolic Conservation Laws," AIAA Paper 85-0363, Jan. 1985.

[25] Anderson, W. K., Thomas, J. L., and Van Leer, B., "A Comparison of Finite Volume Flux Vector Splitting for the Euler Equations," AIAA Paper 85-0122, Jan. 1985.

[26] Jameson, A., Schmidt, W., and Turkel, E., "Numerical Solutions of the Euler Equations by Finite Volume Methods Using Runge-Kutta Time-Stepping," AIAA Paper 81-1259, June 1981.

[27] Yamane, T., and Nagashima, T., "High Speed Centrifugal Impeller and Diffuser Interaction near Stall Condition," *Unsteady Aerodynamics and Aeroelasticity of Turbomachines*, Kluwer Academic Publishers, Dordrecht, The Netherlands, 1998, pp. 259–271.

[28] Yamane, T., Gu, C., and Nagashima, T., "Unsteady Flow Simulation of Centrifugal Impeller and Splitter Interactions," International Symposium on Air Breathing Engines (ISABE) Paper 99-7222, Sept. 1999.

[29] Ikoma, T., Nagashima, T., and Obata, S., "Emissions at Scramjet Engine External Nozzle by Detailed Hydrogen-Air Kinetic Reaction Model," International Symposium on Air Breathing Engines (ISABE) Paper 99-7126, Sept. 1999.

[30] Yamane, T., "The Transplantation of an Unsteady Navier-Stokes Solver for Cascade Flows onto the NWT System," *Parallel Computational Fluid Dynamics: New Algorithms and Applications*, Elsevier Science B.V., Amsterdam, 1995, pp. 137–144.

[31] Yamane, T., and Nagashima, T., "Flow Choking and Shock Wave Structure at Diffuser Vanes in a High Speed Centrifugal Compressor," International Symposium on Air Breathing Engines (ISABE) Paper 95-7011, Vol. 1, 1995, pp. 135–145.

[32] Yamane, T., Fujita, H., and Nagashima, T., "Transonic Discharge Flows Around Diffuser Vanes from a Centrifugal Impeller," International Symposium on Air Breathing Engines (ISABE) Paper 93-7053, 1993, pp. 563–571.

[33] Yamane, T., and Nagashima, T., "A Numerical Study in Three Dimensional Viscous Flows of a Radial-Inflow Turbine," International Symposium on Air Breathing Engines (ISABE) Paper 91-7044, 1991, pp. 439–446.

[34] Toro, E. F., *Riemann Solvers and Numerical Methods for Fluid Dynamics*, Springer, New York, 1997.

C. Tan
Associate Editor